RESEARCH PAPER

Wave Propagation in Biological Tissue with Hyperbolic Two-Temperature and Temperature Dependent Effects under MGT Model

Kunal Sharma ^a, Marin Marin ^{b, c,*}, Rajneesh Kumar ^d

^a Cheminde Chandieu 25,1006 Lausanne, Switzerland
 ^b Department of Mathematics and Computer Science, Transilyania University of Brasov, 500036 Brasov, Romania
 ^c Academy of Romanian Scientists, Ilfov Street, 3, 050045 Bucharest, Romania
 ^d Department of Mathematics, Kurukshetra University, Kurukshetra 136119, Haryana, India

Abstract

This paper presents a theoretical study on the reflection of plane waves in a homogeneous, isotropic bio-thermoelastic diffusion half-space incorporating hyperbolic two-temperature (HTT) effects within the framework of Moore-Gibson-Thompson (MGT) heat conduction. The analysis is performed in two dimensions using dimensionless variables and potential function techniques to simplify the governing equations. Employing normal mode analysis, the study identifies the existence of four distinct longitudinal wave types and a single shear vertical (SV) wave, each propagating with different phase velocities. Analytical expressions for the amplitude ratios corresponding to longitudinal (P), thermal (T), chemical potential (Po), and shear vertical (SV) waves are derived and explored as functions of the incident angle, wave frequency, and relevant material parameters. The effects of the HTT parameter, blood perfusion rate, and various thermoelastic theories on the reflection coefficients are investigated through graphical illustrations. Several special cases are also discussed. The findings are relevant to applications in geomechanics, ocean engineering, and biomedical diagnostics, offering valuable insights into wave behavior in bio-thermoelastic diffusion media under the influence of HTT and MGT models. This work contributes a multiscale framework for studying wave propagation in such complex environments.

Keywords: Bio-thermoelastcity; Diffusion; HTT, MGT heat equation, Impedance boundaries, Amplitude ratios.

1. Introduction

Modelling heat transfer in biological tissues poses significant challenges due to the intricate interaction of thermal and physiological phenomena. These include thermal conduction through various tissue layers, convective effects due to blood circulation, metabolic heat generation, the vascular network's complexity, and the dependency

^{*} Corresponding author. E-mail address: m.marin@unitbv.ro

of thermal and mechanical properties on the tissue's physiological state. Developing accurate mathematical models is crucial for capturing these dynamics, especially in soft tissues, as such models play a vital role in understanding injury mechanisms, enhancing medical diagnostics, and optimizing therapeutic interventions. Additionally, they offer insights into how localized variations impact the overall response of both healthy and pathological tissues.

The foundation of generalized thermoelasticity was laid by Lord and Shulman [1], who introduced a theory incorporating thermal relaxation time by modifying Fourier's law through the Maxwell-Cattaneo approach. This was followed by the model of Green and Lindsay [2], which introduced two distinct relaxation times associated with entropy and stress. Abouelregal and Marin [3] applied the State-Space Method together with the modified couple stress theory to examine the influence of TDP on nanobeam behavior. Sharma et al. [4] investigated fundamental theorems and plane wave propagation in thermoelastic diffusion with a multiphase-lag model that includes temperature dependence. Numerous researchers have employed these advanced heat conduction and diffusion theories to investigate various physical phenomena. For instance, Sharma and Marin [5] studied the impact of different temperature definitions in micropolar thermoelastic systems. Marin et al. [6] employed Lagrange-type identities to establish the uniqueness and instability of solutions within the MGT thermoelastic theory. More recently, Sharma, Marin, and Altenbach [7] considered non-local and phase-lag effects in thermoelastic diffusion, while Marin et al. [8] analyzed fundamental solutions and Green's functions in photothermoelastic media, incorporating temperature-dependent material properties under the MGT model. Hobiny et al. [9] explored the role of hyperbolic two-temperature (HTT) effects on wave propagation in semiconductor materials featuring spherical cavities. The works of Kumar, Ghangas, and Vashishth [10, 11] focused on wave dynamics at the boundary between elastic and bio-thermoelastic media. Impedance boundary conditions have gained considerable attention in theoretical and applied physics, especially in areas such as acoustics and electromagnetism. These boundaries act as transitional zones between perfectly free and rigid interfaces, significantly affecting how waves are transmitted or reflected. Acoustic impedance, in particular, quantifies a material's resistance to wave motion. Numerous studies [12-17] have explored wave reflection and transmission under various impedance conditions. Kumar et al. [17] studied wave propagation in porous thermoelastic media with dual-phase behavior.

This study aims to analyze the reflection of plane waves in a bio-thermoelastic diffusion half-space under the MGT heat conduction model, considering an impedance boundary. Amplitude ratios for various wave types are derived and analyzed based on wave frequency and material properties. The role of blood perfusion is also examined, and several limiting cases are presented to highlight the model's versatility.

2. Governing equations

The mathematical formulation of wave propagation in a bio-thermoelastic diffusion medium is based on the constitutive and field equations that incorporate the effects of thermal and mass diffusion, along with the Moore-Gibson-Thompson (MGT) heat conduction model. In this analysis, the governing equations are simplified by neglecting body forces, internal heat sources, and mass diffusion sources, in accordance with the formulations provided in previous work (see Kumar et al. [11]):

constitutive relation

$$t_{ij} = 2\mu e_{ij} + \delta_{ij}(\lambda_o e_{kk} - \gamma_1 \theta - \gamma_2 P), \tag{1}$$

equation of motion

$$(\lambda_o + \mu)u_{j,ij} + \mu u_{i,jj} - \gamma_1 \theta_{,i} - \gamma_2 P_{,i} = \rho \frac{\partial^2 u_i}{\partial t^2},$$
 (2)

heat conduction equation
$$\left(K \frac{\partial}{\partial t} + K^* \right) \theta_{,ii} = \left(1 + \tau_o \frac{\partial}{\partial t} \right) \left(T_o l \ddot{\theta} + \gamma_1 T_o \ddot{e}_{kk} + dT_o \ddot{P} + \rho_b C_b \omega_b \dot{\theta} \right),$$
 equation of mass diffusion (3)

$$\left(D\frac{\partial}{\partial t} + D^*\right)P_{,ii} = \left(1 + \tau_1 \frac{\partial}{\partial t}\right) \left(n\ddot{P} + \gamma_2 \ddot{e}_{kk} + d\ddot{\theta}\right), \tag{4}$$

$$\ddot{\theta} = \ddot{\varphi} - \beta^* \nabla^2 \varphi,\tag{5}$$

where

$$\lambda_o = \lambda - \frac{\beta_2^2}{b}, \ \gamma_1 = \beta_1 + \beta_2 d, \ \gamma_2 = \frac{\beta_2}{b}, \ d = \frac{a}{b}, n = \frac{1}{b}, \ 1 = \frac{\rho C_e}{T_o} + \frac{a^2}{b}.$$

2.1. Definitions and Parameters

Let the temperature increment be denoted by $T=\theta-T_0$, where θ is the actual temperature within the biological tissue and T_0 is a constant reference temperature. This increment is assumed to be small, such that the relative change $\|(\theta-T_0)/T_0\|$.

The relevant physical parameters are listed below:

- ρ: Mass density of the biological tissue
- Ce: Specific heat capacity at constant strain
- ω_b: Rate of blood perfusion
- ρ_b: Blood density
- c_b: Specific heat capacity of blood
- τ_0 , τ_1 : Phase lag parameters corresponding to heat flux and temperature gradient, respectively
- P: Chemical potential per unit mass
- K: Thermal conductivity
- K*: Modified or effective thermal conductivity
- D: Thermoelastic diffusion coefficient
- D*: Coefficient representing diffusion rate
- a: Thermoelastic diffusion coupling coefficient
- b: Parameter indicating intensity of diffusion-related effects
- β^* : Heat-thermal transfer (HTT) parameter
- t_{ij}: Components of the stress tensor
- u_i: Components of the displacement vector

The coupling effects due to thermal and diffusion processes are given by:

- β_1 =(3 λ +2 μ) α_t , where α_t is the thermal expansion coefficient
- $\beta 2=(3\lambda+2\mu) \alpha_c$, where α_c is the diffusion expansion coefficient

Here, λ and μ denote the Lame parameters. Partial derivatives with respect to spatial coordinates are indicated by a subscript comma followed by the coordinate index, while time derivatives are represented using an overdot.

To examine the influence of temperature dependent material properties we consider $\lambda_0 = \lambda_{o1} f(T)$, $\mu = \mu_o f(T)$, $K = K_o f(T)$, $K^* = K_o^* f(T)$, $K = K_o f(T)$, K

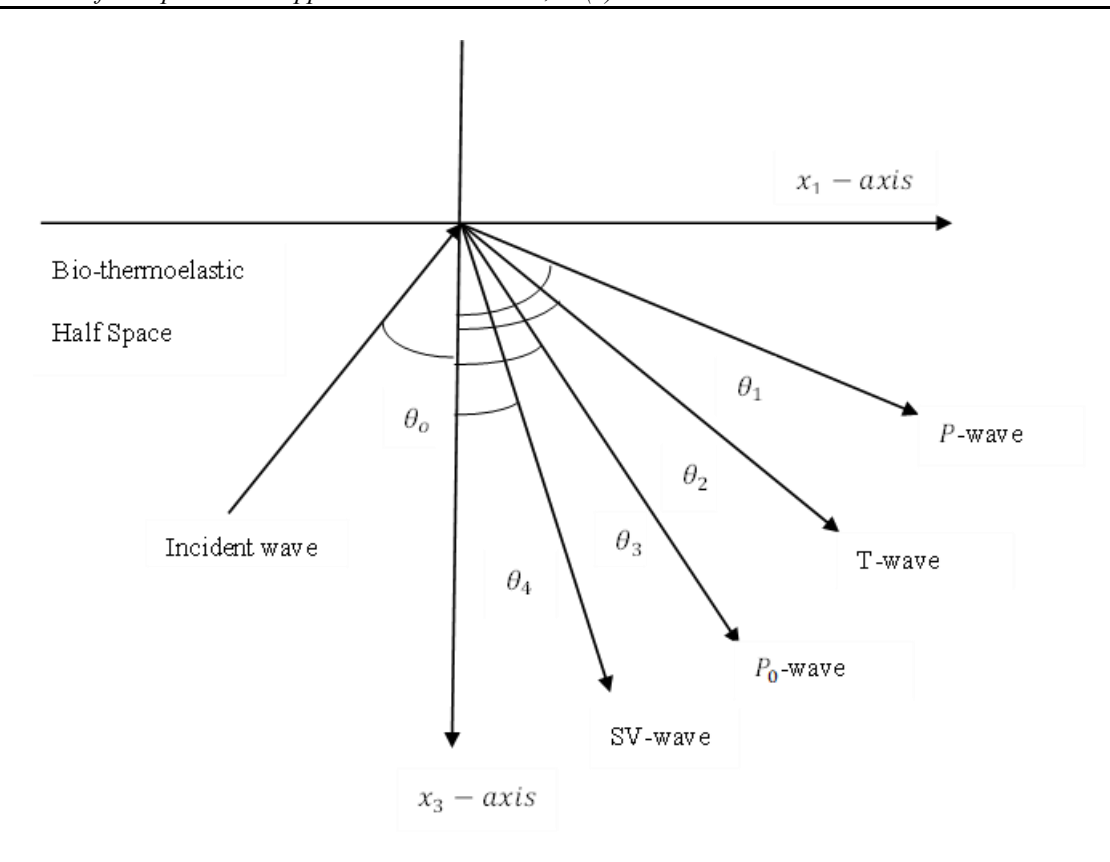


Fig.1. bio-thermoelastic solid half-space

3. Solution procedure

The analysis considers a homogeneous and isotropic bio-thermoelastic diffusion half-space governed by the Moore-Gibson-Thompson (MGT) heat conduction model, incorporating hyperbolic two-temperature (HTT) effects. The medium is defined in a Cartesian coordinate system (x_1, x_2, x_3) , where the boundary surface is situated at $x_3 = 0$, and the half-space extends indefinitely in the positive x₃ direction.

To simplify the problem, wave motion is restricted to the x_1-x_3 plane, assuming that the wavefronts are aligned parallel to the x₂-axis. As a result, all field variables such as the displacement components, temperature increment, and chemical potential are assumed to be functions of the spatial coordinates x₁, x₂, and time t only. This assumption reduces the problem to a two-dimensional framework, facilitating analytical treatment.

$$u = (u_1(x_1, x_3, t), 0, u_3(x_1, x_3, t)), \ \theta(x_1, x_3, t), \ P(x_1, x_3, t).$$
 (6)

By substituting (6) in equations (1)-(5), we obtain the modified system

$$(\lambda_{o1} + \mu_o)\frac{\partial e}{\partial x_1} + \mu_o \nabla^2 u_1 - \gamma_{1o}\frac{\partial \theta}{\partial x_1} - \gamma_{2o}\frac{\partial P}{\partial x_1} = \rho \frac{1}{f(T)}\frac{\partial^2 u_1}{\partial t^2},\tag{7}$$

$$(\lambda_{o1} + \mu_o) \frac{\partial e}{\partial x_3} + \mu_o u_3 - \gamma_{1o} \frac{\partial \theta}{\partial x_3} - \gamma_{2o} \frac{\partial P}{\partial x_3} = \rho \frac{1}{f(T)} \frac{\partial^2 u_3}{\partial t^2}, \tag{8}$$

$$(\lambda_{o1} + \mu_o) \frac{\partial e}{\partial x_3} + \mu_o u_3 - \gamma_{1o} \frac{\partial \theta}{\partial x_3} - \gamma_{2o} \frac{\partial P}{\partial x_3} = \rho \frac{1}{f(T)} \frac{\partial^2 u_3}{\partial t^2},$$

$$f(T) \left(K_o \frac{\partial}{\partial t} + K_o^* \right) \nabla^2 \varphi = \left(1 + \tau_o \frac{\partial}{\partial t} \right) (T_o l \frac{\partial^2 \theta}{\partial t^2} + \gamma_{1o} T_0 f(T) \frac{\partial^2 e}{\partial t^2} + d T_o \frac{\partial^2 P}{\partial t^2} + \rho_b C_b \omega_b \frac{\partial \theta}{\partial t})$$
(8)

$$f(T)\left(D_o\frac{\partial}{\partial t} + D_o^*\right)\nabla^2 P = \left(1 + \tau_1\frac{\partial}{\partial t}\right)\left(n\frac{\partial^2 P}{\partial t^2} + \gamma_{2o}f(T)\frac{\partial^2 e}{\partial t^2} + d\frac{\partial^2 \theta}{\partial t^2}\right),\tag{10}$$

$$\ddot{\theta} = \ddot{\varphi} - \beta^* \nabla^2 \varphi, \tag{11}$$

$$t_{33} = f(T)((\lambda_o + 2\mu_o)u_{3,3} + \lambda_o u_{1,1} - \gamma_{1o}\theta - \gamma_2 P), \tag{12}$$

$$t_{31} = \mu_0 f(T) \left(\frac{\partial u_1}{\partial x_2} + \frac{\partial u_3}{\partial x_1} \right), \tag{13}$$

$$e = \frac{\partial u_1}{\partial x_1} + \frac{\partial u_3}{\partial x_2}, \nabla^2 = \frac{\partial^2 u_1}{\partial x_1^2} + \frac{\partial^2 u_3}{\partial x_3^2}.$$

$$(x'_{i}, u'_{i}) = \frac{\omega_{1}^{*}}{c_{1}} (x_{i}, u_{i}), \qquad (t', \tau'_{o}, \tau'_{1}) = \omega_{1}^{*} (t, \tau_{0}, \tau_{1}), \quad (\theta', \phi') = \frac{\gamma_{1o}}{\rho c_{1}^{2}} (\theta, \phi), \quad P' = \frac{1}{\gamma_{2o} b} P,$$

$$(Z'_{1}, Z'_{2}) = \frac{c_{1}}{\gamma_{1o} T_{o}} (Z_{1}, Z_{2}), \qquad Z'_{3} = \frac{c_{1}}{K_{o}} Z_{3}, \qquad Z'_{4} = \frac{c_{1}}{D_{o}} Z_{4}, \qquad t'_{ij} = \frac{t_{ij}}{\gamma_{1o} T_{o}},$$

where:
$$\omega_1^* = \frac{\rho C_e C_1^2}{K_0}$$
, $C_1^2 = \frac{\lambda_{o1} + 2\mu_o}{\rho}$. (14)

Utilizing equations (14) into equations (7) - (13), the following expressions are obtained

$$f_{11}\frac{\partial e}{\partial x_1} + f_{12}\nabla^2 u_1 - \frac{\partial \theta}{\partial x_1} - f_{13}\frac{\partial P}{\partial x_1} = \frac{1}{f(T)}\frac{\partial^2 u_1}{\partial t^2},\tag{15}$$

$$f_{11}\frac{\partial e}{\partial x_3} + f_{12}\nabla^2 u_3 - \frac{\partial \theta}{\partial x_3} - f_{13}\frac{\partial P}{\partial x_3} = \frac{1}{f(T)}\frac{\partial^2 u_3}{\partial t^2},\tag{16}$$

$$f(T)\left(\frac{\partial}{\partial t} + f_{14}\right)\nabla^{2}\varphi = \left(1 + \tau_{o}\frac{\partial}{\partial t}\right)\left(f_{15}\frac{\partial^{2}\theta}{\partial t^{2}} + f_{16}f(T)\frac{\partial^{2}e}{\partial t^{2}} + f_{17}\frac{\partial^{2}P}{\partial t^{2}} + f_{18}\frac{\partial\theta}{\partial t}\right),\tag{17}$$

$$f(T)\left(\frac{\partial}{\partial t} + f_{19}\right)\nabla^2 P = \left(1 + \tau_1 \frac{\partial}{\partial t}\right) \left(f_{20} \frac{\partial^2 P}{\partial t^2} + f_{21} f(T) \frac{\partial^2 e}{\partial t^2} + f_{22} \frac{\partial^2 \theta}{\partial t^2}\right),\tag{18}$$

$$\ddot{\theta} = \ddot{\ddot{\varphi}} - \beta^* \nabla^2 \ddot{\varphi},\tag{19}$$

$$\ddot{\theta} = \ddot{\ddot{\varphi}} - \beta^* \nabla^2 \ddot{\varphi},$$

$$t_{33} = f_{24} \frac{\partial u_3}{\partial x_3} + f_{23} \frac{\partial u_1}{\partial x_1} - f_{25} \theta - f_{26} P,$$

$$(19)$$

$$(20)$$

$$t_{31} = f_{27} \left(\frac{\partial u_1}{\partial x_2} + \frac{\partial u_3}{\partial x_1} \right), \tag{21}$$

where f_i (i=11-27) are given in Appendix-I.

Using the Helmholtz decomposition, the displacement components u_1 and u_3 can be expressed as follows.

$$u_1 = \frac{\partial \phi}{\partial x_1} - \frac{\partial \psi}{\partial x_3}, \quad u_3 = \frac{\partial \phi}{\partial x_3} + \frac{\partial \psi}{\partial x_1}.$$
 (22)

By substituting equation (22) into equations (15)-(18) and (20)-(21), we obtain:

$$(\nabla^2 - \frac{1}{f(T)} \frac{\partial^2}{\partial t^2}) \phi - \theta - f_{13} P = 0, \tag{23}$$

$$(\nabla^2 - \frac{1}{f(T)} \frac{1}{f_{12}} \frac{\partial^2}{\partial t^2}) \psi = 0, \tag{24}$$

$$f(T)\left(\frac{\partial}{\partial t} + f_{14}\right)\nabla^2\varphi = \left(1 + \tau_o \frac{\partial}{\partial t}\right)\left(f_{15}\frac{\partial^2\theta}{\partial t^2} + f_{16}f(T)\frac{\partial^2\nabla^2\phi}{\partial t^2} + f_{17}\frac{\partial^2P}{\partial t^2} + f_{18}\frac{\partial\theta}{\partial t}\right),\tag{25}$$

$$f(T)\left(\frac{\partial}{\partial t} + f_{19}\right)\nabla^2 P = \left(1 + \tau_1 \frac{\partial}{\partial t}\right) \left(f_{20} \frac{\partial^2 P}{\partial t^2} + f_{21} f(T) \frac{\partial^2 \nabla^2 \phi}{\partial t^2} + f_{22} \frac{\partial^2 \theta}{\partial t^2}\right),\tag{26}$$

$$t_{33} = (f_{24} - f_{23}) \frac{\partial^2}{\partial x_1 \partial x_3} \psi + f_{24} \frac{\partial^2 \phi}{\partial x_3^2} + f_{23} \frac{\partial^2 \phi}{\partial x_1^2} - f_{25} \theta - f_{26} P, \tag{27}$$

$$t_{31} = 2f_{27} \frac{\partial^2 \emptyset}{\partial x_1 \partial x_3} + f_{27} \left(\frac{\partial^2}{\partial x_1^2} - \frac{\partial^2}{\partial x_1^2}\right) \psi, \tag{28}$$

4. Wave Propagation Analysis

We examine the propagation of plane waves in a bio-thermoelastic solid half-space that incorporates the hyperbolic two-temperature (HTT) model and is governed by the Moore–Gibson–Thompson (MGT) heat conduction equation. This half-space is bounded at a surface, and when a wave is incident upon it, several reflected wave components are generated. These include a longitudinal wave (P-wave), a thermal wave (T-wave), a chemical potential wave (Powave), and a vertically polarized shear wave (SV-wave), as depicted schematically in Figure 1.

Assuming harmonic plane wave propagation, where the wave normal lies in the $x_1 - x_3$ plane and forms an angle

 θ_0 with the positive x_3 -axis (which is perpendicular to the boundary surface), the solution to equations (23)–(26) is assumed to take the following form:

$$(\phi, \psi, \varphi, \theta, P) = (\phi^o, \psi^o, \varphi^o, \theta^o, P^o)e^{ik(x_1sin\theta_o - x_3cos\theta_o + \theta t)}$$
(29)

Here, ϕ^o , ψ^o , ϕ^o , θ^o , P^o are arbitrary constants representing the amplitudes of the respective wave components.

The parameter k denotes the wave number, and θ is the phase velocity of the propagating wave.

By substituting equation (29) into equations (23)–(26), and utilizing equation (19), we arrive at the following algebraic system

$$(C_{11}\vartheta^6 + C_{12}\vartheta^4 + C_{13}\vartheta^2 + C_{14})(\phi^o, \varphi^o, P^o) = 0,$$

$$(\vartheta^2 - f(T)f_{12})\psi^o = 0$$
(30)

The roots ϑ_i (i=1, 2, 3) of the characteristic equation

$$(C_{11}\vartheta^6 + C_{12}\vartheta^4 + C_{13}\vartheta^2 + C_{14}) = 0,$$

 $\vartheta_1, \vartheta_2, \vartheta_3$ correspond to the phase velocities of the longitudinal (P-wave), thermal (T-wave), and chemical potential (Po-wave), respectively. The fourth root $\vartheta_4 = \sqrt{f(T)f_{12}}$ represents the phase velocity of the shear vertical (SV-wave). The coefficients C_i (i=11-14) are defined explicitly in Appendix II.

5. Impedance Boundary Conditions

Impedance boundary conditions represent a linear relationship between unknown field variables and their spatial derivatives on a boundary surface. These conditions are widely utilized in various domains of physics, including thermoelasticity, acoustics, and electromagnetics. In the context of seismic wave propagation, it is typically assumed that interfaces exhibit ideally welded contact, implying continuity in both displacement and stress components.

However, for thin interfacial layers or imperfect bonding, this assumption may not hold, and a more appropriate representation involves impedance-type boundary conditions.

The impedance boundary conditions at the surface $x_3 = 0$ can be expressed as:

$$\begin{array}{ll} \text{(i)} & t_{33}+\omega Z_1 u_3=0 \;, \\ \text{(iii)} & K_o \frac{\partial \varphi}{\partial x_3}+\omega Z_3 \varphi=0, \end{array} \\ \text{(iv)} & D_o \frac{\partial P}{\partial x_3}+\omega Z_4 P=0, \end{array} \tag{32}$$

Where Z_1 , Z_2 are impedance parameters with dimension N sec m^{-3} . Z_3 and Z_4 are impedance parameters with dimension N $m^{-1}K^{-1}$ and Ns⁴ m^{-4} respectively. Taking $Z_1 = Z_2 = Z_3 = Z_4 = 0$ yields stress free boundary conditions.

6. Reflection Phenomenon of Waves

We consider an incident P-wave or T-wave or Po-wave or SV-wave, striking the boundary surface at an angle θ_0 with respect to the normal (x_3 -axis), as shown in Fig. 1. When this incident wave interacts with the boundary, it generates four reflected waves corresponding to the same possible modes (P, T, Po, SV). These reflected waves propagate into the medium at angles θ_1 , θ_2 , θ_3 and θ_4 respectively, measured from the positive x_3 -axis. Hence, the total wave field in the medium is expressed as the superposition of the incident wave and all reflected counterparts, each characterized by its own amplitude, direction of propagation, and polarization and is given by

$$\phi = \sum_{j=1}^{3} \{G_{oj} e^{ik_j (x_1 \sin \theta_o - x_3 \cos \theta_o) + i\omega t} + G_j e^{ik_j (x_1 \sin \theta_j + x_3 \cos \theta_j) + i\omega t} \}, \tag{33}$$

$$\varphi = \sum_{j=1}^{3} m_j \Big\{ G_{0j} e^{ik_j (x_1 \sin \theta_0 - x_3 \cos \theta_0) + i\omega t} + G_j e^{ik_j (x_1 \sin \theta_j + x_3 \cos \theta_j) + i\omega t} \Big\}, \tag{34}$$

$$P = \sum_{j=1}^{3} n_j \left\{ G_{oj} e^{ik_j (x_1 \sin \theta_0 - x_3 \cos \theta_0) + i\omega t} + G_j e^{ik_j (x_1 \sin \theta_j + x_3 \cos \theta_j) + i\omega t} \right\}.$$

$$\psi = G_{o4} e^{ik_j (x_1 \sin \theta_0 - x_3 \cos \theta_0) + i\omega t} + G_4 e^{ik_4 (x_1 \sin \theta_4 + x_3 \cos \theta_4) + i\omega t},$$
(35)

$$\psi = G_{04}e^{ik_j(x_1\sin\theta_0 - x_3\cos\theta_0) + i\omega t} + G_4e^{ik_4(x_1\sin\theta_4 + x_3\cos\theta_4) + i\omega t},$$
(36)

In these expressions:

- $G_{oj}(j=1, 2, 3)$ represent the amplitudes of the incident longitudinal (P), thermal (T), and chemical potential (P_o) waves, respectively.
- G_{04} denotes the amplitude of the incident shear vertical (SV) wave.
- G(j=1, 2, 3) correspond to the amplitudes of the reflected P, T, and Po waves.
- G₄ is the amplitude of the reflected SV wave.
- m_i and f_i (j=1,2,3) are coupling constants, whose explicit forms are provided in Appendix III.
- n_i denote the wave numbers associated with the respective wave types, and ω is the angular frequency of wave propagation.

These components collectively characterize the total field resulting from the superposition of incident and reflected waves within the bio-thermoelastic solid, modelled using the hyperbolic two-temperature (HTT) framework in conjunction with the Moore–Gibson–Thompson (MGT) heat conduction equation.

$$\frac{\sin \theta_{o}}{v_{o}} = \frac{\sin \theta_{j}}{v_{j}},$$
where
$$k_{j}v_{j} = \omega, \text{ at } x_{3} = 0 \text{ (j= 1, 2, 3, 4)},$$

$$v_{0} = \begin{cases}
v_{1}, & \text{for incident } P - wave, \\
v_{2}, & \text{for incident } T - wave, \\
v_{3}, & \text{for incident } P_{o} - wave, \\
v_{4}, & \text{for incident } SV - wave.
\end{cases}$$
(37)

By substituting the expressions for the potential functions from equations (33) - (36), along with equation (19), into the boundary conditions given in equation (32), and employing the relations from equations (27) and (28), we derive the following system of equations:

$$\sum F_{ij}R_j = Y_j, \qquad (i, j=1, 2, 3, 4).$$
 where F_{ij} , R_j and Y_j are given in Appendix-IV (38)

7. Particular Cases

i. In absence of blood perfusion

By setting $\omega_h = 0$ in equation (38), the model simplifies to the case of thermoelastic diffusion with TDP in the

absence of blood perfusion. This reduction yields the governing equations for a bio-thermoelastic medium incorporating hyperbolic two-temperature (HTT) and TDP effects within the framework of the Moore–Gibson–Thompson (MGT) heat conduction model.

ii. Absence of temperature dependent parameters

Taking $\alpha^*=0$ in equation (38), yield the corresponding results for bio-thermoelasic diffusion with HTT and MGT model.

iii. Absence of diffusion.

If
$$\boldsymbol{\beta}_{2} = \boldsymbol{a} = \boldsymbol{D} = \boldsymbol{D}^{*} = \boldsymbol{n} = \boldsymbol{0} \text{ in eq. (30), gives.}$$

$$(P_{12}\vartheta^{4} + (P_{11} - P_{12} - P_{13})\vartheta^{2} + P_{13})(\boldsymbol{\phi}, \ \boldsymbol{\varphi}) = 0,$$
where
$$P_{11} = -P_{10}f(T)f_{16}, P_{12} = P_{10}\left(f_{15} - \frac{i}{\omega}f_{18}\right)(1 - \zeta^{*}K^{2}),$$

$$P_{13} = (i\omega + f_{14})f(T), \qquad P_{10} = (1 + i\omega\tau_{o}).$$
(39)

In this scenario, the boundary conditions specified in equation (32) take the following form:

(i)
$$t_{33} + \omega Z_1 u_3 = 0$$
, (ii) $t_{31} + \omega Z_2 u_1 = 0$, (iii) $\frac{\partial \varphi}{\partial x_3} + \omega Z_3 \varphi = 0$. (40)

By applying the same procedure, the system of equations presented in equation (38) simplifies to the following form:

$$\sum F_{ij}^{O} R_{j}^{O} = Y_{i}^{O}, \qquad (i, j=1, 2, 3),$$
where F_{ij}^{O} , R_{j}^{O} and Y_{j}^{O} are given in Appendix-V. (41)

In the case where diffusion effects are neglected, the relevant terms associated with chemical potential and mass transport are omitted. The resulting model then describes wave propagation in a thermoelastic medium governed temperature dependent properties under the HTT and MGT formulations

iv. Absence of thermal effect.

Taking
$$\beta_1 = c_e = c_b = K = K^* = 0$$
 in eq. (30), we obtain $(P_{22}\vartheta^4 + (P_{21} - P_{23})\vartheta^2 + P_{23})(\phi, P) = 0,$ (42) where:
$$P_{21} = -P_{20}f_{21}f(T)$$

 $P_{22} = P_{20}f_{21}(1 - \zeta^*K^2), P_{23} = (i\omega + f_{19}), P_{20} = (1 + i\omega\tau_1)f(T),$

The boundary conditions outlined in equation (32) can be explicitly written as follows:

(i)
$$t_{33} + \omega Z_1 u_3 = 0$$
, (ii) $t_{31} + \omega Z_2 u_1 = 0$, (iii) $\frac{\partial P}{\partial x_3} + \omega Z_4 P = 0$. (43)

Following as above, the system of equation (38) reduces of the form

$$\sum F_{ij}^{00} R_j^{00} = Y_i^{00}, \qquad (i, j=1, 2, 3),$$
where F_{ij}^{00} , R_j^{00} and Y_j^{00} are given in Appendix-VI

v. Absence of Impedance Parameters (Z1=Z2=Z3=Z4=0)

In this case, the boundary conditions from equation (32) simplify to:

(i)
$$t_{33} = 0$$
, (ii) $t_{31} = 0$, (iii) $\frac{\partial \varphi}{\partial x_3} = 0$, (iv) $\frac{\partial P}{\partial x_3} = 0$. (45) Therefore, we obtain
$$\sum F_{ij}^{O1} R_j^{O1} = Y_i^{O1}, \quad (i, j=1, 2, 3, 4),$$
 where F_{ij}^{O1} , R_j^{O1} and Y_j^{O1} are given in Appendix-VII

The deduced results for all the above cases are in agreement, if we solve the problem directly.

8. Numerical result and discussion

Following the work of Li et al. [19], the values of the physical constants used in the numerical computations are as follows:

$$\begin{array}{lll} \lambda_0 = 2.696 \times 10^{10} Kgm^{-1}s^{-2}, & \mu = 1.639 \times 10^{10} Kgm^{-1}, & \rho = 1.74 \times 10^3 Kgm^{-3}, \\ T_0 = 0.293 K & , & c_e = 1.04 \times 10^3 JKg^{-1} & , & \alpha_T = .0178 \times 10^{-5} K^{-1} & , \\ \alpha_C = .0198 \times 10^{-4} Kg^{-1}m^3 & , & a = 1.02 \times 10^4 m^2 K^{-1}s^{-2} & , & b = 9 \times 10^5 Kg^{-1}m^5s^{-2} & , \\ K = 1.7 \times 10^2 Wm^{-1} K^{-1}, D^* = 1.4W/mks, D = 0.85 \times 10^{-8} Kgm^{-3}s, & D^* = 0.65 Kgsm^{-3}, \omega \\ = 1. & \rho_b = 1.060 Kgm^{-3}, & c_b = 3600 JKg^{-1} K^{-1}, & \omega_b = 1.87 \times 10^{-3} s^{-1} \\ \tau_o = 0.2sec, \tau_1 = 0.4sec & \end{array}$$

In Figures 2(a-d), 3(a-d) and 4(a-d): (ω_b =1.87, ζ^* =.25, Z_1 =5, Z_2 =10, Z_3 =15, Z_4 =20)

- The solid line represents bio-thermoelastic diffusion using the temperature dependent property (TDP) model with Moore–Gibson–Thompson (MGT) heat conduction, where α^* =.3.
- The dotted line corresponds to bio-thermoelastic diffusion with the temperature dependent property (TDP)) model under MGT heat conduction, with α^* =.5.
- The dashed line depicts bio-thermoelastic diffusion with the temperature dependent property (TDP) and MGT model when α*=0.

In Figures 5(a-d), 6(a-d) and 7(a-d): (
$$\omega_b$$
=1.87, α^* =.3, Z_1 =10, Z_2 =20, Z_3 =30, Z_4 =40)

- The solid line represents bio-thermoelastic diffusion using the hyperbolic two-temperature (HTT) model with Moore–Gibson–Thompson (MGT) heat conduction, where ζ^* =.5.
- The dotted line corresponds to bio-thermoelastic diffusion with the two-temperature (2TT) model under MGT heat conduction, with ζ*=.25.
- The dashed line depicts bio-thermoelastic diffusion with the HTT and MGT model when $\zeta^*=0$.

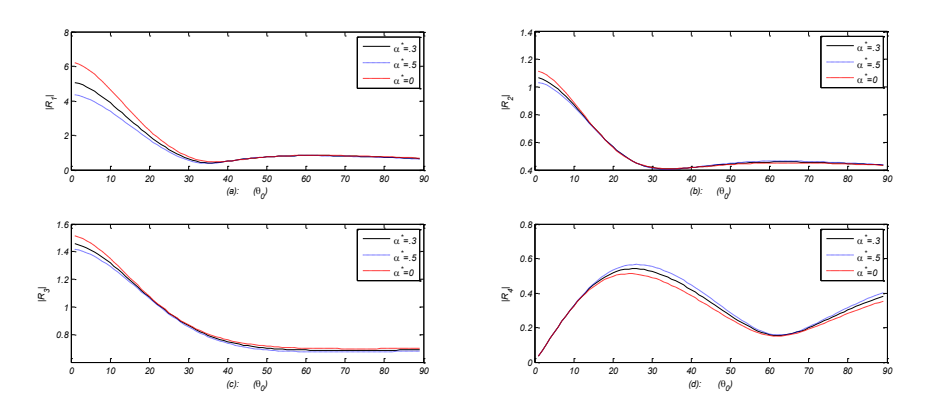
In Figures 8(a-d), 9(a-d), and 10(a-d):
$$(\zeta^* = .5, \alpha^* = .3, Z_1=10, Z_2=20, Z_3=30, Z_4=40)$$

- The dotted line corresponds to bio-thermoelastic diffusion with HTT and MGT considering blood perfusion parameter ω_b =2.5.
- The solid line represents bio-thermoelastic diffusion with HTT and MGT for ω_b =1.5.
- The dashed line shows the model results when blood perfusion is neglected $\omega_b=0$.

In Figures 11(a-d), 12(a-d), and 13(a-d): (
$$\zeta$$
=.5, ω_b =1.87, =.3)

- The solid line represents bio-thermoelastic diffusion with HTT under the Moore–Gibson–Thompson (MGT) model including impedance parameters Z1=10,Z2=20,Z3=30,Z4=40.
- The dashed line illustrates the same model without impedance effects (Z1=Z2=Z3=Z4=0).
- The dotted line shows results based on the Lord–Shulman (LS) thermoelastic theory with HTT, including the same impedance parameters Z1=10,Z2=20,Z3=30,Z4=40

8.1. Effect of α^* (TDP parameter)



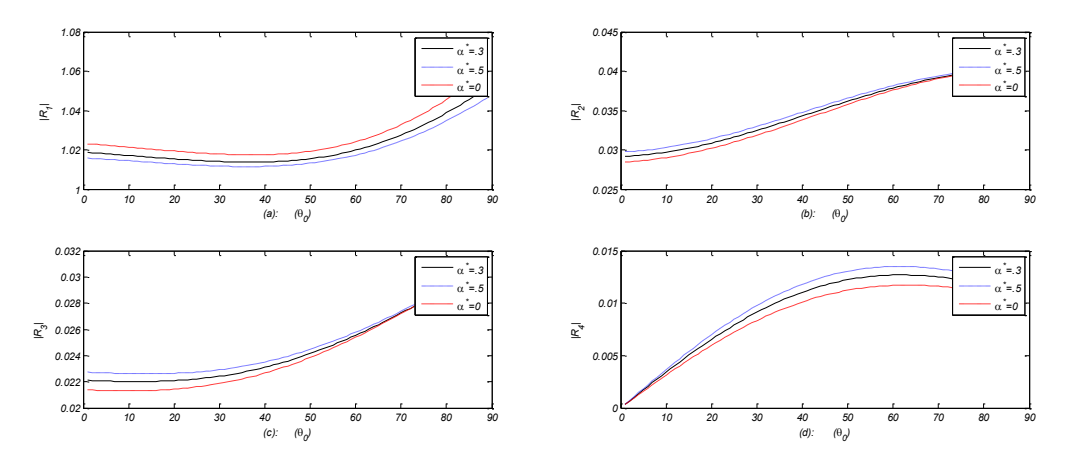
Fig(2a-2d): Effect of α^* on Amplitude Ratios for Incident P-Wave.

Figure 2a demonstrates the variation of $|R_1|$ vs θ_o . For all three cases of the temperature dependent parameter $(\alpha^* = .3, .5, 0)$, $|R_1|$ initially decreases in the interval $0 \le 0 \le 35 \circ$. Beyond this range, $|R_1|$ exhibits a gradual increase, with only slight differences in magnitude across the three models. This behavior suggests that the reflection characteristics of the longitudinal wave are moderately sensitive to the value of α^* , particularly at larger incident angles.

Figure 2b illustrates the response of $|R_2|$ vs θ_o . In this case, $|R_2|$ decreases monotonically within the range $0 \le \theta_o \le 32$. After this point, $|R_2|$ begins to increase slightly as the angle of incidence grows. The trend is consistent for all values of α^* , but the rate of variation differs subtly, indicating that thermal coupling influences the reflected thermal wave more prominently at higher angles of incidence.

Figure 2(c) shows the variation of $|R_3|$ vs θ_o . Unlike the previous cases, the amplitude ratio decreases monotonically across the entire angular range for all three models. The magnitude of $|R_3|$ differs significantly depending on the choice of α^* , highlighting a distinct sensitivity of the chemical potential wave reflection to the temperature dependent parameter.

Figure 2(d) illustrates the variation of $|R_4|$ vs θ_o . $|R_4|$ increases within the angular interval $0 \le \theta_o \le 22$, after which it decreases until $\theta \circ \approx 63 \circ$. Beyond this point, $|R_4|$ again exhibits an increasing trend. Among the three cases, the model with $\alpha^* = .5$ a attains the highest peak amplitude compared to $\alpha^* = .3$, and 0

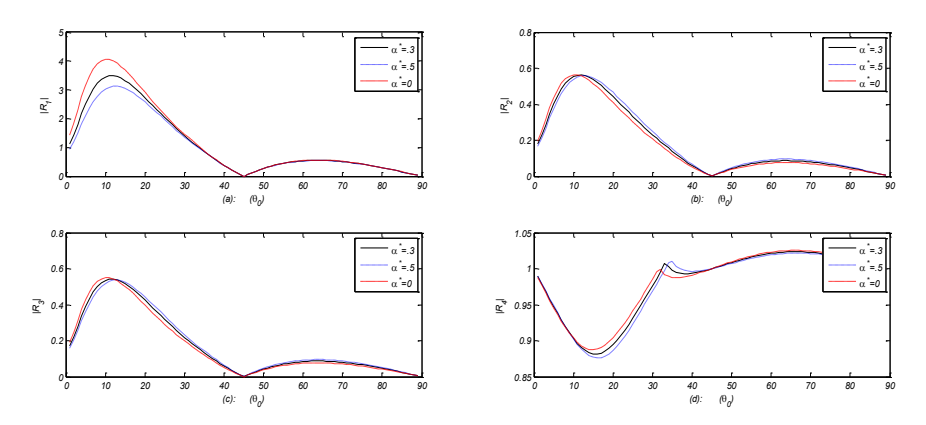


Fig(3a-3d): Effect of α^* on Amplitude Ratios for Incident T-Wave.

Figure 3a shows the behavior of $|R_1|$ vs θ_o . For all three values of the TDP parameter ($\alpha^* = .3, .5$ and 0), the amplitude ratio decreases within the interval $0 \le \theta_o \le 40$. Beyond this range, $|R_1|$ begins to rise monotonically, eventually attaining a nearly uniform peak at larger angles.

Figures 3b,c display the variation of $|R_2|$ & $|R_3|$ vs θ_o . In both cases, the amplitude ratios increase monotonically as the angle of incidence advances. The growth is more pronounced at higher angles, and distinct magnitudes are observed among the three models, with $\alpha^* = .5$ generally producing the strongest response.

Figure 3(d) depicts the behavior of $|R_4|$ vs θ_o . The amplitude ratio $|R_4|$ increases steadily within the range $0 \le \theta_o \le 60$. However, beyond $\theta_o \approx 60$ °, the trend reverses, and $|R_4|$ begins to decrease. This non-monotonic pattern highlights a critical angle beyond which the reflection of the SV-wave weaken.



Fig(4a-4d): Effect of α^* on Amplitude Ratios for Incident SV-wave.

Figure 4a shows the variation of $|R_1|$ vs θ_o . For all values $\alpha^*=.3,.5$ and 0,the amplitude $|R_1|$ initially increases within the interval $0 \le \theta_o \le 12$. This is followed by a decreasing trend up to $\theta_o = 45$, after which $|R_1|$ again advances in the range $45 \le \theta_o \le 65$. Beyond $\theta_o \ge 65$, the amplitude ratio decreases. The maximum reflection is observed for $\alpha^*=0$, while the lowest magnitude occurs at $\theta = 0$. This indicates that longitudinal wave reflection under SV-wave incidence is highly sensitive to both angle and α^*

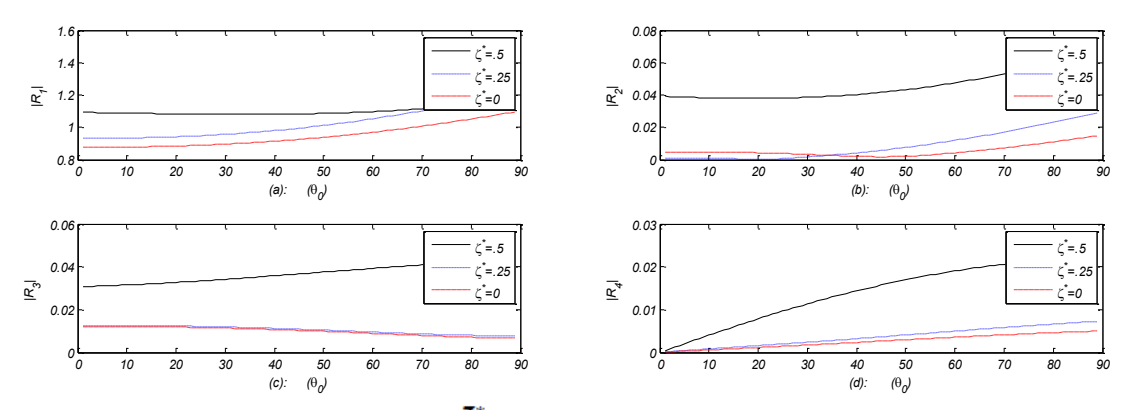
The amplitude ratios $|R_1|$, $|R_2|$ & $|R_3|$ for advances $0 \le \theta_o \le 12$ and $45 \le \theta_o \le 65$ beyond its starts decreasing $12 \le \theta_o \le 45$ and $\theta_o \ge 65$ and attain higher peak for $\alpha^* = 0$ and lower magnitude for all cases at $\theta_o = 0$.

Figure 4b shows the variation of $|R_2|$ vs θ_o . $|R_2|$ exhibits a similar trend to $|R_1|$. The values of $|R_2|$ increase in the range $0 \le \theta_o \le 12$, decrease monotonically within $12 \le \theta_o \le 45$, and rise again up to $\theta_o \approx 65$. Beyond this angle, a decreasing trend is observed. Among the models, $\alpha^* = 0$ shows the highest amplitude ratio, while the cases with $\alpha^* = .3$ and $\alpha^* = .5$ yield comparatively smaller magnitudes.

Figure 4b illustrates the variation of $|R_3|$ vs θ_o . The response $|R_3|$ is nearly identical to that of $|R_1|$ and $|R_2|$, with growth in the intervals $0 \le \theta_o \le 12$ and $45 \le \theta_o \le 65$, and decline in the intermediate and higher angular ranges. The magnitude of $|R_3|$ attains its highest peak for $\alpha^*=0$, while the values for $\alpha^*=.3$ and $\alpha^*=.5$ remain comparatively lower.

Figure 4d depicts the changes of $|R_4|$ vs θ_o . Unlike the earlier cases, $|R_4|$ decreases slightly in the range $0 \le \theta_o \le 15$, then increases within $15 \le \theta_o \le 30$, and again for $\theta_o \ge 35$. At higher angles, $|R_4|$ approaches a nearly uniform value, indicating stabilization. The differences in magnitudes of $|R_4|$ for $\alpha^* = .3$, .5 and 0 is significant although small.

8.2 Effect of **ζ***(HTT,2TT,1T)



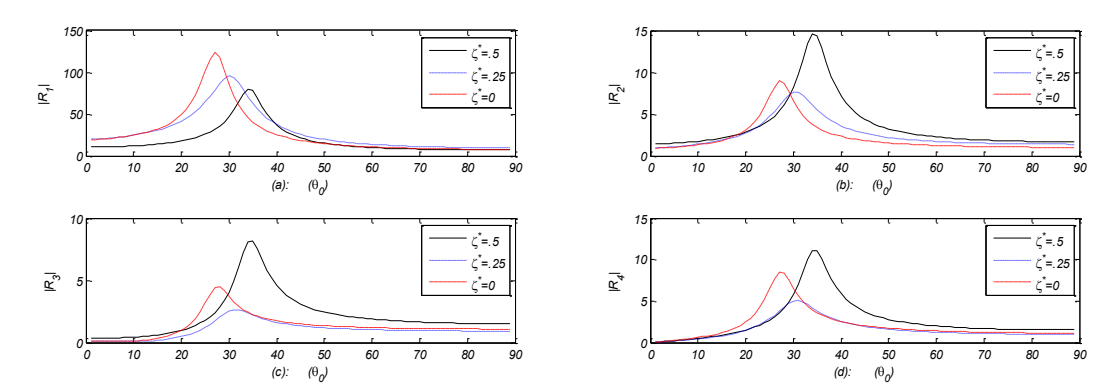
Fig(5a-5d): Effect of ζ^* on Amplitude Ratios for Incident P-Wave.

Figure 5a demonstrate the variation of $|R_1|$ vs θ_o . Amplitude ratios R_1 increases with distinct magnitude as angle of incidence increases for all models. $|R_1|$ attains higher magnitude for HTT in comparison to 2TT & 1T models.

Figure 5b shows behavior of $|R_2|$ vs θ_o . The values of $|R_2|$ remains higher for HTT in contrast to 2TT & 1T. The value of $|R_2|$ advances with low magnitudes for 2TT & 1T for $0 \le \theta_o \le 40$ and as $\theta_o > 40$, $|R_2|$ advances with higher magnitude.

Figure 5c display the variation of $|R_3|$ vs θ_o . The value of $|R_3|$ for 2TT & 1T advances with lower magnitude for all values of θ_o . $|R_3|$ advances as θ_o advances for HTT attaing the higher values in contrast to 2TT & 1T models.

Figure 5d shows the variation of $|R_4|$ vs θ_o . $|R_4|$ increases continuously as θ_o increases for HTT with significant difference of magnitude in comparision to 2TT & 1T. $|R_4|$ attains lower value in case of 1T although $|R_4|$ increases as θ_o increases for both 2TT & 1T cases.



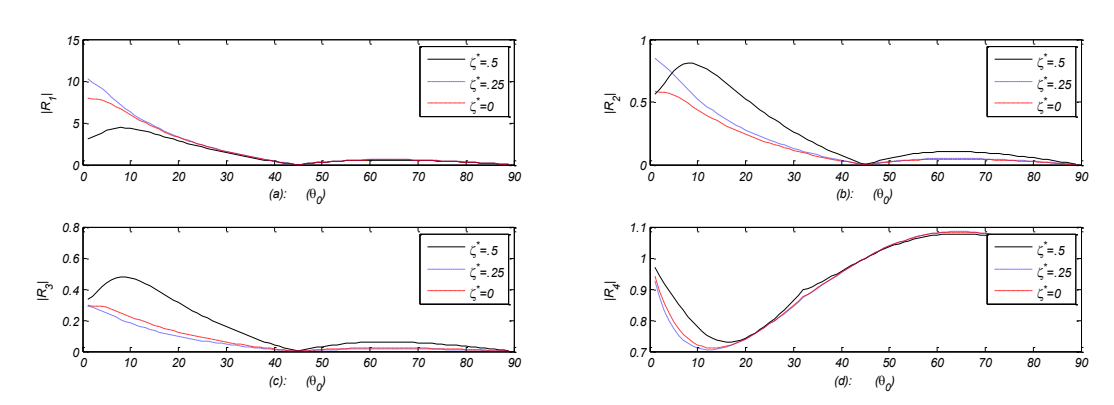
Fig(6a-6d): Effect of ζ^* on Amplitude Ratios for Incident T-Wave.

Figure 6a display variation of $|R_1|$ vs θ_o . The plot shows increasing trends for all the cases, attaing peak values and then decreases as θ_o increases. $|R_1|$ attains lower values for HTT as $0 \le \theta_o \le 32$. As $\theta_o \ge 45$, the values of $|R_1|$ advances with similar variations.

Figure 6b shows variation of $|R_2|$ vs θ_o . $|R_2|$ increases with small variation attains peak values and decreases as θ_o advances for all the models. Magnitude of $|R_2|$ remains higher for HTT in compare to other models 2TT & 1T models as $\theta_o \ge 30$.

Figure 6c display variation of $|R_3|$ vs θ_o . $|R_3|$ for HTT increases monotonically, attaing higher magnitude and then decreases as angle increases. The curves for $|R_3|$ in 2TT & 1T models attain lower peak in contrast to HTT models. As $\theta_o \ge 32$, the value of $|R_3|$ for 2TT & 1T curves closed to each other.

Fig.6d display variation of $|R_4|$ vs θ_o . $|R_4|$ attains higher magnitude for HTT in contrast to other models. $|R_4|$ remains higher for 2TT in comparison to 1T as $0 \le \theta_o \le 20$ and then advances with small difference of magnitude as θ_o increases further. Under T-wave incidence, thermal effects (HTT and 2TT) introduce slight variations mainly at low frequencies, with HTT ($\zeta^* = 5$) showing marginally elevated and oscillatory amplitudes. As frequency increases, differences between HTT, 2TT, and 1T models diminish, indicating weaker thermal sensitivity for SV wave compared to P- and T-wave cases.



Fig(7a-7d): Effect of ζ^* on Amplitude Ratios for Incident SV-Wave

Figure 7a shows variation of $|R_1|$ vs θ_o . For lower values of θ_o , $|R_1|$ attains maximum for all the models. $|R_1|$ goes on decreases attaining minima and again increases with slight variation for HTT, 2TT, 1T. The magnitude of $|R_1|$ remains lower for HTT in comparison to others models for $0 \le \theta_o \le 30$.

Fig.7b depicts variation of $|R_2|$ vs θ_o . The value of $|R_2|$ for 2TT lies between HTT & 1T for $4 \le \theta_o \le 40$. As $\theta_o > 40$, $|R_2|$ attains higher magnitude for 2TT in comparison to HTT & IT.

Fig.7c demonstrate variation of $|R_3|$ vs θ_o . Magnitude of $|R_3|$ remains higher for HTT in comparison to 2TT & 1T. The behavior and variation of $|R_3|$ for all models is similar with distinct magnitude as $\theta_o > 40$.

Fig.7d display variation of $|R_4|$ vs θ_o . $|R_4|$ decreases monotonically and then increases as θ_o advances for all

the models. $|R_4|$ attains higher magnitude for HTT in comparison to other models.

8.2. Effect of blood perfusion parameter $\omega_{\mathbf{h}}$

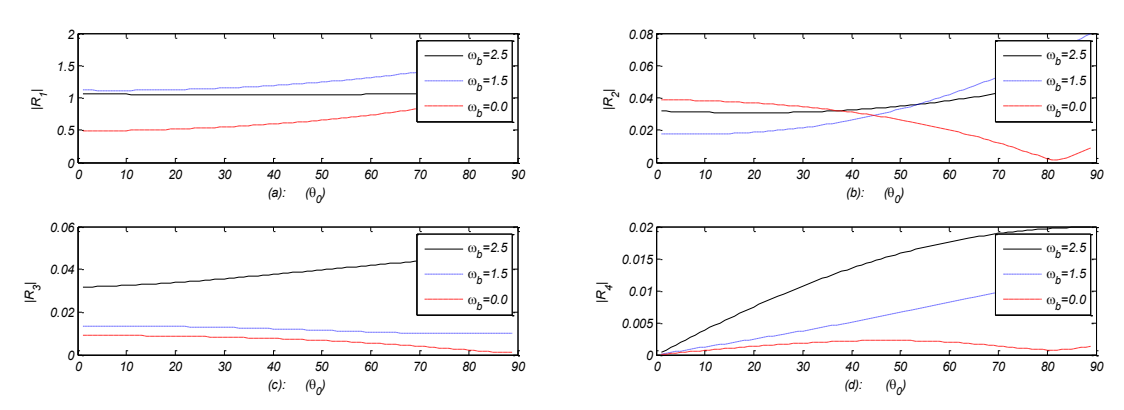


Fig.8 (a- d): Analyzing the Role of ω_b in Modulating Amplitude Ratios (P-Wave)

Figure 8a display the changes of $|R_1|$ vs θ_o . For all three cases, $|R_1|$ increases gradually with angle. The rate of increase is most significant for $\omega_b=2.5$, followed by $\omega_b=1.5$, while the case $\omega_b=0$ shows a more beguiling change. This indicates that higher blood perfusion intensity enhances the angular sensitivity of $|R_1|$.

Figure 8b shows variations of $|R_2|$ vs θ_o . For $\omega_b=2.5$, 1.5 the amplitude $|R_2|$ increases after a moderate initial slope, reaching its peak at higher angles. For $\omega_b=0$, $|R_2|$ initially rises slightly and then exhibits a downward trend at larger angles.

Figure 8c presents the variations of $|R_3|$ with θ_o . All three cases show a steady and monotonic increase in the magnitude of $|R_3|$, with the strongest rise occurring at $\omega_b=2.5$. The increase is less pronounced for $\omega_b=1.5$, while in case of $\omega_b=0$ remains relatively flat.

Figure 8d depicts the behaviour of R_4 with θ_o . For $\omega_b=2.5$, there is a rapid and continuous rise in $|R_4|$ across the full angular range, implying strong reflection behavior at high blood perfusion rate. A similar but gentler trend is seen for $\omega_b=1.5$ whereast, the response for $\omega_b=0$ shows only a mild increase before leveling off.

Figure 9a illustrates the variation of $|R_1|$ with respect to θ_o . For $\omega_b=2.5$, $|R_1|$ decreases slightly as θ_o increases, while for $\omega_b=1.5$, it exhibits a slight increasing trend. In the absence of blood perfusion $\omega_b=0$, $|R_1|$ increases in the range $0 \le \theta_o \le 13$, and then begins to decrease for $\theta_o \ge 13$.

Figure 9b presents the behaviour of $|R_2|$ vs θ_o . The amplitude $|R_2|$ for $\omega_b=2.5$ decreases monotonically with increasing θ_o . In contrast, $|R_2|$ for $\omega_b=1.5$ and $\omega_b=0$ increases with varying magnitudes.

Fig. 9c display the changes of $|R_3|$ vs θ_o . For the higher blood perfusion rate $\omega_b=2.5$, $|R_3|$ increases and eventually attains a uniform value. For $\omega_b=1.5$ and $\omega_b=0$, $|R_3|$ also increases, but with different magnitudes.

Figure 9d depicts the changes in $|R_4|$ vs θ_0 . For $\omega_b = 2.5$ and $\omega_b = 1.5$, $|R_4|$ increases with distinct

magnitudes. For $\omega_b = 0$, R_4 increases up to the midpoint of the region beyond which it shows a slight downward trend.

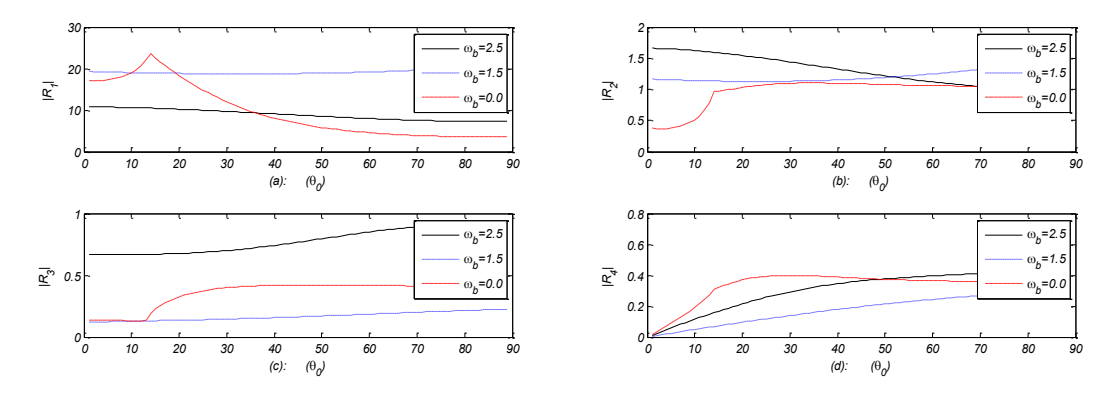


Fig. 9 (a, b, c, d): Analyzing the Role of ω_b in Modulating Amplitude Ratios (T-Wave)

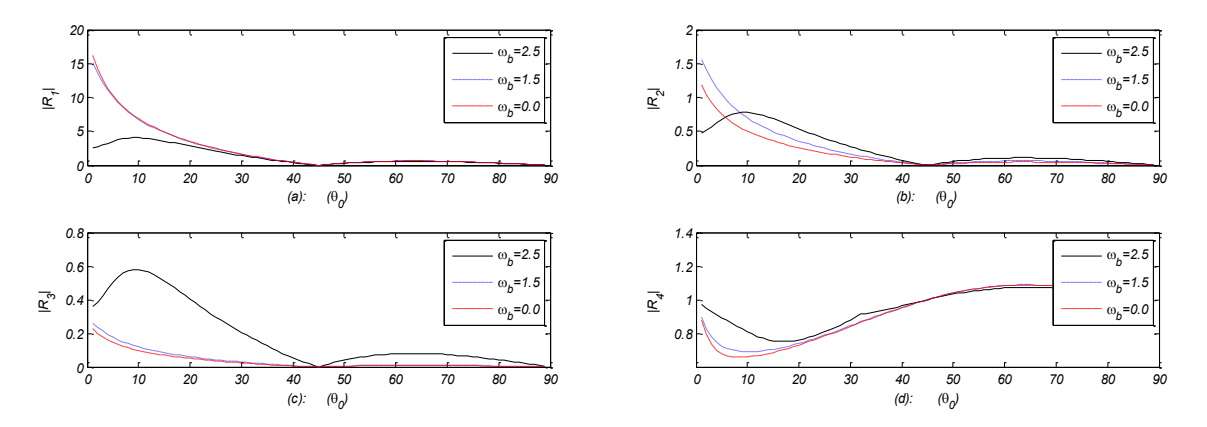


Fig. 10(a, b, c, d): Analyzing the Role of ω_b in Modulating Amplitude Ratios (SV-Wave)

Fig.10a illustrates the variation of $|R_1|$ vs θ_o . For $\omega_b=2.5$, $|R_1|$ increases within the range $0 \le \theta_o \le 10$ and decreases at $10 \le \theta_o \le 45$ beyond it starts increasing slightly. $|R_1|$ for $\omega_b=1.5$ and 0 decreases and attains its lower magnitude in the middle of the region beyond its starts increasing slightly.

Fig.10b display the changes of $|R_2|$ vs θ_o . $|R_2|$ for ω_b =2.5 increases at $0 \le \theta_o \le 10$ and $45 \le \theta_o \le 65$ and rest is decreasing.

Fig.10c depicts the trend of $|R_3|$ vs θ_o . The amplitude $|R_3|$ for ω_b =2.5 increases in the range $0 \le \theta_o \le 10$ and $45 \le \theta_o \le 65$ beyond its starts decreasing in $10 \le \theta_o \le 45$ and $65 \le \theta_o \le 90$. $|R_3|$ for ω_b =1.5 and 0 decreases slightly as the value of θ_o increases.

Fig.10d presents the variation of $|R_4|$ vs θ_o . The amplitude $|R_4|$ for ω_b =2.5 decreases at $0 \le \theta_o \le 10$, followed by gradual increase as θ_o increases. In case of ω_b =1.5 and 0, $|R_4|$ decreases within the interval $0 \le \theta_o \le 6$, beyond its starts increasing.

Fig.11a demonstrates the variation of $|R_1|$ vs θ_o . The demeanour and alteration of $|R_1|$ for MGI and LSI is stable with slight difference in magnitude. $|R_1|$ for MGWI increases monotonically in the range $0 \le \theta_o \le 65$ beyond its starts decreasing.

Fig.11b display the changes of $|R_2|$ vs θ_o . The amplitude $|R_2|$ for MGI and LSI exhibit a slight downward trend differing mainly in magnitude. $|R_2|$ for MGWI shows a gradual increase for $0 \le \theta_o \le 65$ after which it begins to decline.

Fig.11c presents the changes in $|R_3|$ vs θ_o . The amplitude $|R_3|$ for MGI and LSI decreases at the range

 $0 \le \theta_o \le 10$ beyond its starts increasing and attains its uniform magnitude. $|R_3|$ for MGWI increases at the range $0 \le \theta_o \le 65$ beyond it starts decreases monotonically.

Fig.11d illustrates the response of $|R_4|$ vs θ_o . The amplitude $|R_4|$ for MGI and LSI reveals a steadily increasing trend which eventually levels off to a nearly constant value. $|R_4|$ for MGWI increases slightly at the range $0 \le \theta_o \le 60$ and rest is decreasing.

8.3. Comparison of thermoelastic theories and impendence impact.

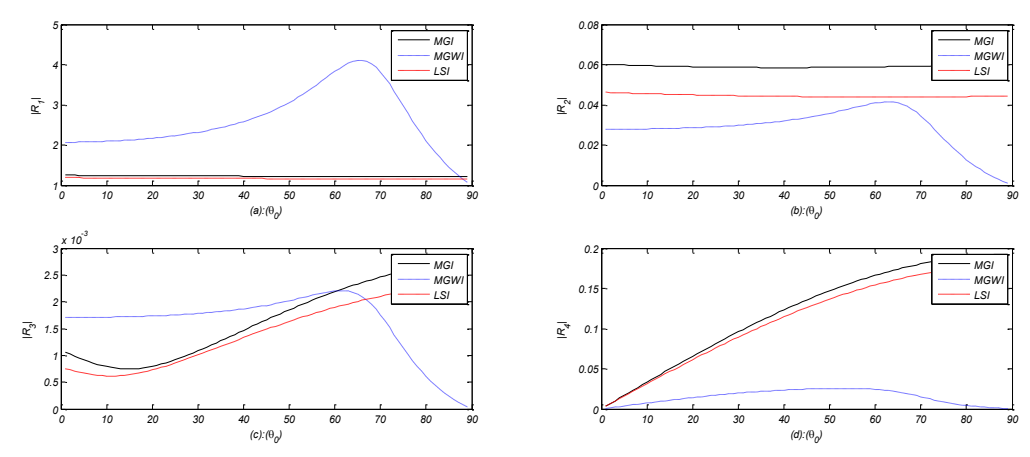


Fig.11 (a, b, c, d): Incident P-Wave Interaction with Impedance Boundaries in Varied Thermoelastic Frameworks.

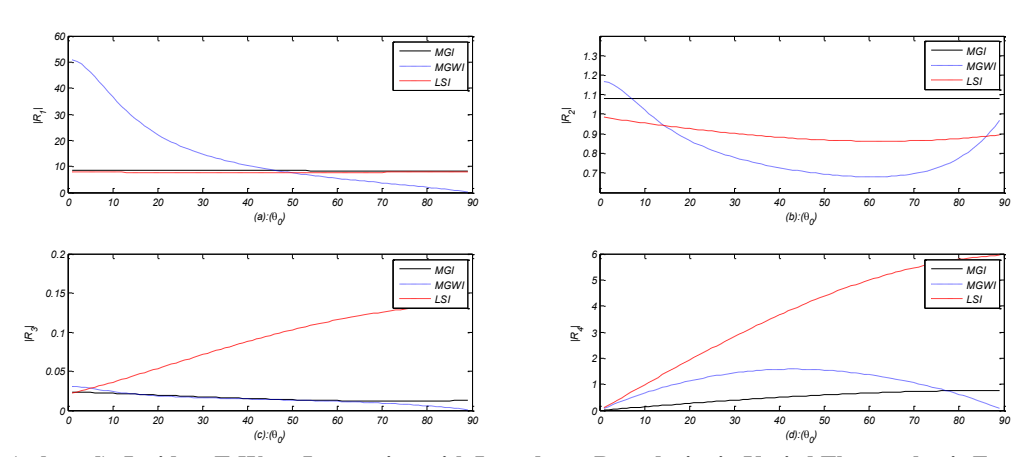


Fig.12 (a, b, c, d): Incident T-Wave Interaction with Impedance Boundaries in Varied Thermoelastic Frameworks.

Fig.12a display the changes of $|R_1|$ vs θ_o . The behaviour and variation of R_1 for MGI and LSI is stable with slight difference in magnitude. $|R_1|$ for MGWI is monotonically decreases as the value of θ_o increases.

Fig.12b display the changes of $|R_2|$ vs θ_o . $|R_2|$ for MGI remains stable whereas for LSI first decreases slightly and then increases gradually. $|R_2|$ for MGWI decreases within the range $0 \le \theta_o \le 60$ beyond it starts increases as θ_o increases.

Fig.12c display the changes of $|R_3|$ vs θ_o . $|R_3|$ for MGI and MGWI decrease gradually with increasing angle. $|R_3|$ for LSI increases monotonically and attaining its uniform magnitude.

Fig.12d display the changes of $|R_4|$ vs θ_o . $|R_4|$ for MGI increases slightly. $|R_4|$ for for MGWI increases at

low angle, reaches maximum and the decreases at highest angle and in this case $|R_4|$ has a parabolic -shaped curve. $|R_4|$ has a moderate increasing trend for LSI and is more stable in comparison to other cases.

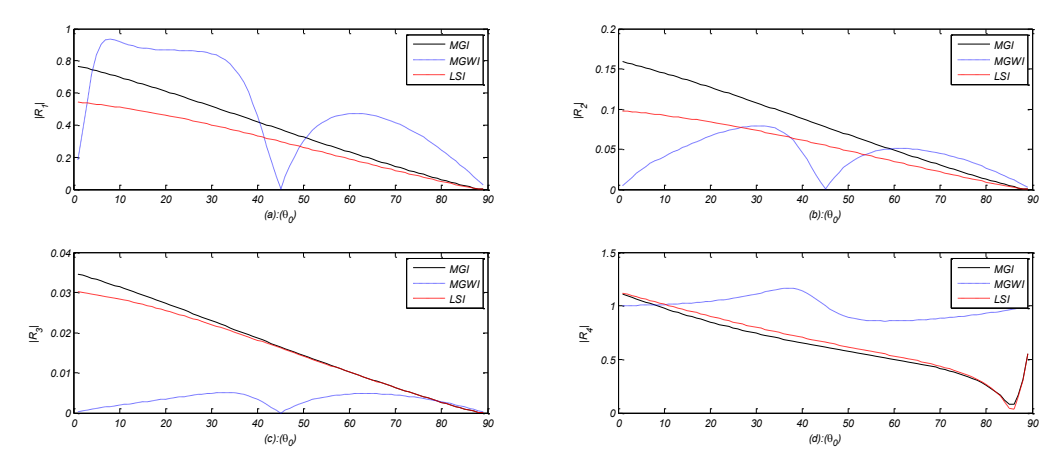


Fig. 13 (a, b, c, d): Incident SV-Wave Interaction with Impedance Boundaries in Varied Thermoelastic Frameworks

Fig.13a display the changes of $|R_1|$, vs θ_o . $|R_1|$ decrease monotonically as angle of incidence increases for MGI and LSI models, although the curves for both cases are smooth and closely parallel, declining toward a low but non zero value at the largest angle. $|R_1|$ for MGWI model display a strong oscillator pattern throughout the angular range. Fig.13b depicts the variation of $|R_2|$ vs θ_o . $|R_2|$ shows a steady, monotonic decrease with increasing θ_o for MGI and LSI although decline is smooth to a consistent low magnitude. $|R_2|$, for MGWI continues to oscillate attaining minima at 45^0 angle. Fig.13c demonstrates changes of $|R_3|$ vs θ_o . $|R_3|$ consistently decreases monotonically, mirroring each other closely for both the models MGI and LSI. $|R_3|$ for MGWI depicts a pronounced oscillatory trend, markedly different from the smooth decay of the other models .Fig.13d shows the variation of $|R_4|$ vs θ_o . The amplitude $|R_4|$ decreases within the interval $0 \le \theta_o \le 85$, followed by a gentle increase toward 90^0 for MGI and LSI models although with distinct pattern. $|R_4|$ for MGWI remains oscillatory across all angles attaining maximum value at highest angle.

9. Conclusion

This study investigates the reflection behavior of plane waves in a bio-thermoelastic diffusion half-space incorporating hyperbolic two-temperature (HTT) effects, modelled using the Moore–Gibson–Thompson (MGT) heat conduction theory. The governing equations were established in two dimensions and subsequently simplified through the introduction of dimensionless variables and potential functions. Amplitude ratios for various reflected wave modes were derived subject to impedance boundary conditions. Numerical simulations were performed, and the results were graphically analyzed to examine the influences of HTT, blood perfusion rates, and different thermoelastic theories on the wave reflection characteristics. The main conclusions drawn from this analysis are summarized as follows:

9.1. Effect of α*

From the obtained numerical results, it is observed that the temperature-dependent parameter α^* plays a significant role in governing the reflection characteristics of different wave modes. The reflection amplitudes $|R_1|$, $|R_2|$, $|R_3|$ generally decrease at smaller incident angles and increase beyond certain angular thresholds, with noticeable

differences in magnitude across the three models. The case $\alpha^*=0.5$ often produces higher peaks compared to $\alpha^*=0.3$ and $\alpha^*=0$, demonstrating the strengthening effect of temperature dependent parameter.

For $|R_4|$, the response is more complex, showing non-monotonic variation with angle. While $\alpha^*=0.5$ tends to enhance peak values, the overall sensitivity of $|R_4|$, to α^* effects is smaller than that of the other modes.

Overall, the results indicate that increasing α^* amplifies reflection in most cases, particularly for longitudinal, thermal, and chemical potential waves, while SV-wave reflection is only moderately affected.

9.2. Effect of ₹*

The amplitude ratios for reflected waves under P-wave incidence are significantly influenced by the thermal models employed. The HTT ($\zeta^* = .5$) model exhibits the highest amplitude reflecting the strong influence of hyperbolic thermal effects. 2TT ($\zeta^* = .25$) model yields moderate amplitude ratios, capturing the dual temperature impact while damping wave reflection to some extent. 1T ($\zeta^* = 0$) model results in the lowest amplitude ratios, due to the absence of thermal relaxation, indicating less energy transfer across the boundary

For T-wave incidence, the amplitude ratios are notably affected by the thermal models. The Hyperbolic Two-Temperature (HTT, $\zeta^* = .5$) model exhibits sharp peaks and higher amplitude ratios, indicating strong wave—thermal interactions. The Two-Temperature (2TT, $\zeta^* = .25$), produces moderate amplitude ratios with reduced peak intensity, showing the damping effect of dual-temperature diffusion whereas one-Temperature (1T, $\zeta^* = 0$) model yields lowest amplitude ratios and peak shifts, reflecting minimal thermal feedback and wave energy loss. For SV-wave incidence, the amplitude ratios are moderately affected by the thermal models. The HTT model ($\zeta^* = .5$) shows noticeable fluctuations and higher initial amplitude values, while the 2TT ($\zeta = .25$) model demonstrates a smoother decay with slightly lower amplitude ratios, reflecting the damping influence of dual-temperature effects. 1T ($\zeta^* = 0$) model exhibits minimal amplitude variation, closely approaching the classical elastic response with negligible thermal interaction

9.3. Effect of wb.

The analysis reveals that the blood perfusion rate significantly influences all the amplitude ratios under P-wave incidence. As ω_b increases, all amplitude ratios exhibit enhanced angular sensitivity and magnitude. Higher values of ω_b lead to steeper and more pronounced increases in reflection amplitudes, indicating stronger wave interaction with the medium. Conversely, for ω_b =0, the amplitude ratios show weaker variation and reduced reflection behavior.

For T-wave incidence, the amplitude ratios are notably influenced by the blood perfusion rate ω_b Higher value of ω_b generally leads to smoother or saturating behavior in amplitude variations, while moderate blood perfusion ($\omega_b = 1.5$) yields gradual increases. In contrast, the absence of perfusion ($\omega_b = 0$) results in more irregular and angle-sensitive responses.

Under SV-wave incidence, the amplitude ratios exhibit distinct angular behaviors influenced by the blood perfusion rate ω_b . For high perfusion (ω_b =2.5), the amplitude ratios display more complex, piecewise trends with alternating increases and decreases across angular ranges. In contrast, ω_b =1.5 and ω_b =0, the amplitude ratios show simpler, more gradual variations—typically with initial decreases followed by mild increases.

9.4. Impact of impedance and comparison of different theories of thermoelasticity:

The impedance boundary conditions distinctly affect the amplitude ratios across the thermoelastic models—MGI, LSI, and MGWI. The MGI and LSI models exhibit relatively stable and gradual variations with angle, showing minor differences primarily in magnitude. In contrast, the MGWI model, incorporating relaxation effects, shows pronounced angular sensitivity with noticeable peaks or turning points around θ_0 . $\approx 60^{\circ}-65^{\circ}$.

Under impedance boundary conditions, the amplitude ratios respond differently across the MGI, LSI, and MGWI models. MGI and LSI show generally stable and smooth trends with minor magnitude differences. In contrast, the MGWI model exhibits more dynamic behavior. Under impedance boundary conditions, MGI and LSI models exhibit smooth, monotonic decrease in amplitude ratios. In contrast, the MGWI model shows pronounced oscillatory behavior across all amplitude ratios, with significant fluctuation, which highlights the strong influence of thermal relaxation effects on wave reflection compared to the stable decay in MGI and LSI mode.

Appendix-I

$$f_{11} = \frac{\lambda_{01} + \mu_{o}}{(\lambda_{01} + 2\mu_{o})}, f_{12} = \frac{\mu_{o}}{(\lambda_{01} + 2\mu_{o})}, f_{13} = \frac{\gamma_{2o}^{2} b}{(\lambda_{01} + 2\mu_{o})}, f_{14} = \frac{K_{o}^{*}}{K_{o} \omega_{1}^{*}}, f_{15} = \frac{T_{o} l C_{1}^{2}}{K_{o} \omega_{1}^{*}}, f_{16} = \frac{\gamma_{1o}^{2} T_{o}}{K_{o} \omega_{1}^{*}}, f_{17} = \frac{d T_{o} \gamma_{1o} \gamma_{2o} b}{K_{o} \omega_{1}^{*} \rho}, f_{18} = \frac{\rho_{b} c_{b} \omega_{b} c_{1}^{2}}{K_{o} \omega_{1}^{*}}, f_{19} = \frac{D^{*}}{D \omega_{1}^{*}}, f_{20} = \frac{n c_{1}^{2}}{D \omega_{1}^{*}}, f_{21} = \frac{c_{1}^{2}}{D \omega_{1}^{*} b}, f_{22} = \frac{d c_{1}^{4} \rho}{D \omega_{1}^{*} \gamma_{1o} \gamma_{2o} b}.$$

$$f_{23} = \frac{\lambda_{01}}{T_{o} \gamma_{1o}} f(T), f_{24} = \frac{\lambda_{01} + 2\mu_{o}}{T_{o} \gamma_{1o}} f(T), f_{25} = \frac{\rho c_{1}^{2}}{T_{o} \gamma_{1o}} f(T), f_{26} = \frac{\gamma_{2o}^{2} b}{T_{o} \gamma_{1o}} f(T), f_{27} = \frac{\mu_{o}}{T_{o} \gamma_{1o}} f(T).$$

Appendix-II

$$P_{10} = 1 + i\omega\tau_{o}, \ P_{11} = -P_{10}f_{16}f(T) \quad , \quad P_{12} = P_{10}(f_{15} - \frac{i}{\omega}f_{18} \quad) \quad (1 - \zeta^{*}K^{2})$$

$$P_{13} = (i\omega + f_{14}) f(T), \quad P_{14} = P_{10}f_{17} \quad , \quad P_{20} = 1 + \tau_{1}i\omega, \ P_{21} = -P_{20}f_{21}f(T) \quad , \quad P_{22} = P_{20}f_{22}(1 - \zeta^{*}K^{2})$$

$$P_{23} = P_{20}f_{20}, \quad P_{24} = (i\omega + f_{19}) f(T)$$

$$C_{11} = P_{12}P_{23} - P_{14}P_{22}$$

$$C_{12} = -P_{12}P_{24} - P_{13}P_{23} - P_{12}P_{23}f(T)(1 - \zeta^{*}K^{2}) + P_{14}P_{22}f(T) + P_{14}P_{21}f(T)(1 - \zeta^{*}K^{2}) - f_{13}P_{11}P_{22}f(T) + f_{13}P_{12}P_{21}f(T)$$

$$C_{13} = P_{13}P_{24} + P_{12}P_{24}f(T) + P_{13}P_{23}f(T) - P_{11}P_{24}f(T)(1 - \zeta^{*}K^{2}) - f_{13}P_{13}P_{21}f(T)$$

$$C_{14} = -P_{13}P_{24}f(T),$$

$$\zeta^{*} = \begin{cases} \frac{\beta^{*}}{\omega^{2}} & \text{for hyperbolic two-temperature (HTT)} \\ 0 & \text{for two-temperature (2TT)} \\ 0 & \text{for one temperature (1T)} \end{cases}$$

Appendix-III

$$\begin{split} m_j &= -\frac{(P_{11}P_{23} - P_{14}P_{21})\omega^2\vartheta^2 - P_{11}P_{24}\omega^2}{(P_{12}\vartheta^2 - P_{13})(P_{23}\vartheta^2 - P_{24}) - P_{14}P_{22}\vartheta^4} \\ n_j &= \frac{(P_{11}P_{22} - P_{12}P_{21})\omega^2\vartheta^2 + P_{13}P_{21}\omega^2}{(P_{12}\vartheta^2 - P_{13})(P_{23}\vartheta^2 - P_{24}) - P_{14}P_{22}\vartheta^4} \end{split}$$

Appendix-IV

$$\begin{split} F_{1j} &= -f_{24}k_{j}^{2}cos^{2}\theta_{j} - f_{23}k_{j}^{2}sin^{2}\theta_{j} - f_{25}m_{j} - f_{26}n_{j} + i\omega k_{j}Z_{1}cos\theta_{j} \\ F_{14} &= -(f_{24} - f_{23})k_{4}^{2}sin\theta_{4}cos\theta_{4} + i\omega k_{4}Z_{1}cos\theta_{4} \\ F_{2j} &= -2f_{27}k_{j}^{2}sin\theta_{j}cos\theta_{j} + i\omega k_{j}Z_{2}sin\theta_{j} \\ F_{24} &= -f_{27}k_{4}^{2}sin^{2}\theta_{4} + f_{27}k_{4}^{2}cos^{2}\theta_{4} - iZ_{2}\omega k_{4}cos\theta_{4} \\ F_{3j} &= im_{j}k_{j}\cos\theta_{j} + \omega Z_{3}m_{j} \\ F_{34} &= 0. \end{split}$$

(j=1,

$$F_{4j} = in_j k_j \cos \theta_j + \omega Z_4 n_j$$

 $F_{44} = 0.$
(j=1, 2, 3).

Where R_1, R_2, R_3 and R_4 are the amplitude ratios of reflected P-wave, reflected T-wave, P_0 —wave and SV-wave.

$$R_1 = \frac{G_1}{G^*}, \ R_2 = \frac{G_2}{G^*}, \ R_3 = \frac{G_3}{G^*} \ \text{and} \ R_4 = \frac{G_4}{G^*}.$$

For incident P-Wave:

$$G^* = G_{01} = G_{02} = G_{03} = G_{04} = 0$$

$$Y_1 = f_{24}k_1^2\cos^2\theta_0 + f_{23}k_1^2\sin^2\theta_0 + f_{25}m_1 + f_{26}n_1 + i\omega k_1 Z_1\cos\theta_0$$

$$Y_2 = -2f_{27}k_1^2\sin\theta_0\cos\theta_0 - i\omega k_1 Z_2\sin\theta_0$$

$$Y_3 = i m_1 k_1 \cos \theta_0 - \omega Z_3 m_1$$

$$Y_4 = i n_1 k_1 \cos \theta_O - \omega Z_4 n_1$$

For incident T- wave:

$$G^* = G_{02}, \qquad G_{01} = G_{03} = G_{04} = 0$$

$$Y_1 = f_{24}k_2^2\cos^2\theta_0 + f_{23}k_2^2\sin^2\theta_0 + f_{25}m_2 + f_{26}n_2 + i\omega k_2 Z_1\cos\theta_0$$

$$Y_2 = -2f_{27}k_2^2\sin\theta_0\cos\theta_0 - i\omega k_2 Z_2\sin\theta_0$$

$$Y_3 = i m_2 k_2 \cos \theta_0 - \omega Z_3 m_2$$

$$Y_4 = i n_2 k_2 \cos \theta_0 - \omega Z_4 n_2$$

For incident P_o — Wave:

$$G^* = G_{03}, \qquad G_{01} = G_{02} = G_{04} = 0$$

$$Y_1 = f_{24}k_3^2\cos^2\theta_0 + f_{23}k_3^2\sin^2\theta_0 + f_{25}m_3 + f_{26}n_3 + i\omega k_3 Z_1\cos\theta_0$$

$$Y_2 = -2f_{27}k_3^2\sin\theta_0\cos\theta_0 - i\omega k_3 Z_2\sin\theta_0$$

$$Y_3 = i m_3 k_3 \cos \theta_0 - \omega Z_3 m_3$$

$$Y_4 = i n_3 k_3 \cos \theta_0 - \omega Z_4 n_3$$

For incident SV-Wave:

$$G^* = G_{04}, \qquad G_{01} = G_{02} = G_{03} = 0$$

$$Y_{1} = -(f_{24} - f_{23})k_{4}^{2}\sin\theta_{0}\cos\theta_{0} - i\omega k_{4}Z_{1}\sin\theta_{0}$$

$$Y_2 = f_{27}k_4^2 \sin^2\theta_0 - f_{27}k_4^2 \cos^2\theta_0 + i\omega k_4 Z_2 \cos\theta_0$$

$$Y_3 = 0.$$

$$Y_4=0.$$

Appendix-V

$$F_{1i}^{0} = -f_{24}k_{i}^{2}\cos^{2}\theta_{i} - f_{23}k_{i}^{2}\sin^{2}\theta_{i} - f_{25}m_{i} + i\omega k_{i}Z_{1}\cos\theta_{i}$$

$$F_{13}^{0} = -(f_{24} - f_{23})k_{4}^{2}\sin\theta_{4}\cos\theta_{4} + i\omega k_{4}Z_{1}\cos\theta_{4}$$

$$F_{2j}^{0} = -2f_{27}k_{j}^{2}\sin\theta_{j}\cos\theta_{j} + i\omega k_{j}Z_{2}\sin\theta_{j}$$

$$F_{2i}^{0} = -2f_{27}k_{i}^{2}\sin\theta_{i}\cos\theta_{i} + i\omega k_{i}Z_{2}\sin\theta_{i}$$

$$F_{23}^{0} = -f_{27}k_{4}^{2}\sin^{2}\theta_{4} + f_{27}k_{4}^{2}\cos^{2}\theta_{4} - i\omega k_{4}Z_{2}\cos\theta_{4}$$

$$F_{3i}^{0} = i m_i k_i \cos \theta_i + \omega Z_3 m_i$$

$$F_{33}^0 = 0.$$

2) For incident P-Wave:

$$G^* = G_{01}, \qquad G_{02} = G_{03} = G_{04} = 0$$

$$Y_1^0 = f_{24}k_1^2\cos^2\theta_0 + f_{23}k_1^2\sin^2\theta_0 + f_{25}m_1 + i\omega k_1 Z_1\cos\theta_0$$

$$Y_2^0 = -2f_{27}k_1^2\sin\theta_0\cos\theta_0 - i\omega k_1 Z_2\sin\theta_0$$

$$Y_3^0 = i m_1 k_1 \cos \theta_0 - \omega Z_3 m_1$$

For incident T- wave:

$$G^* = G_{02}, \qquad G_{01} = G_{03} = G_{04} = 0$$

```
Y_1^0 = f_{24}k_2^2\cos^2\theta_0 + f_{23}k_2^2\sin^2\theta_0 + f_{25}m_2 + i\omega k_2 Z_1\cos\theta_0
    Y_2^0 = -2f_{27}k_2^2\sin\theta_0\cos\theta_0 - i\omega k_2 Z_2\sin\theta_0
    Y_3^0 = i m_2 k_2 \cos \theta_0 - \omega Z_3 m_2
    For incident SV-Wave:
    G^* = G_{04}
                           G_{01} = G_{02} = G_{03} = 0
    Y_1^0 = -(f_{24} - f_{23})k_4^2 \sin\theta_0 \cos\theta_0 - i\omega k_4 Z_1 \sin\theta_0
    Y_2^0 = f_{27}k_4^2\sin^2\theta_0 - f_{27}k_4^2\cos^2\theta_0 + i\omega k_4 Z_2\cos\theta_0
    Y_3^0 = 0.
Appendix-VI
    \bar{F}_{1j}^{00} = -f_{24}k_j^2\cos^2\theta_j - f_{23}k_j^2\sin^2\theta_j - f_{26}n_j + i\omega k_j Z_1\cos\theta_j
    F_{13}^{00} = -(f_{24} - f_{23})k_4^2 \sin\theta_4 \cos\theta_4 + i\omega k_4 Z_1 \cos\theta_4
    F_{2j}^{00} = -2f_{27}k_j^2\sin\theta_j\cos\theta_j + i\omega k_j Z_2\sin\theta_j
    F_{23}^{00} = -f_{27}k_{A}^{2}\sin^{2}\theta_{A} + f_{27}k_{A}^{2}\cos^{2}\theta_{A} - i\omega k_{A}Z_{2}\cos\theta_{A}
    F_{3j}^{00} = i n_j k_j \cos \theta_j + \omega Z_4 n_j
    F_{33}^{00} = 0
                                                                                                                                                  j = (1,
2)
    For incident P-Wave:
    G^*=G_{01},
                          G_{02} = G_{03} = G_{04} = 0
    Y_1^{00} = f_{24}k_1^2\cos^2\theta_0 + f_{23}k_1^2\sin^2\theta_0 + f_{26}n_1 + i\omega k_1 Z_1\cos\theta_0
    Y_2^{00} = -2f_{27}k_1^2\sin\theta_0\cos\theta_0 - i\omega k_1Z_2\sin\theta_0
    Y_3^{00} = i n_1 k_1 \cos \theta_0 - \omega Z_4 n_1
    For incident P_0 – Wave:
    G^*=G_{03},
                            G_{01} = G_{02} = G_{04} = 0
    Y_1^{00} = f_{24}k_2^2\cos^2\theta_0 + f_{23}k_2^2\sin^2\theta_0 + f_{26}n_2 + iZ_1\omega k_2\cos\theta_0
    Y_2^{00} = -2f_{27}k_2^2\sin\theta_0\cos\theta_0 - i\omega k_2Z_2\sin\theta_0
    Y_3^{00} = i n_2 k_2 \cos \theta_0 - \omega Z_4 n_2
    For incident SV-Wave:
    G^* = G_{04}, \qquad G_{01} = G_{02} = G_{03} = 0
    Y_1^{00} = -(f_{24} - f_{23})k_4^2 \sin\theta_0 \cos\theta_0 - iZ_1\omega k_4 \sin\theta_0
    Y_2^{00} = f_{27}k_4^2\sin^2\theta_0 - f_{27}k_4^2\cos^2\theta_0 + i\omega k_4 Z_2\cos\theta_0
    Y_3^{00} = 0.
Appendix-VII
    F_{1i}^{01} = -f_{24}k_i^2\cos^2\theta_i - f_{23}k_i^2\sin^2\theta_i - f_{25}m_i - f_{26}n_i
    F_{14}^{01} = -(f_{24} - f_{23})k_4^2 sin\theta_4 cos\theta_4
    F_{2j}^{\tilde{o}1} = -2f_{27}k_j^2\sin\theta_j\cos\theta_i
    F_{24}^{01} = -f_{27}k_4^2\sin^2\theta_4 + f_{27}k_4^2\cos^2\theta_4
    F_{3j}^{O1} = i m_j k_j \cos \theta_j
    F_{34}^{01}=0.
    F_{4j}^{O1} = i n_j k_j \cos \theta_j
    F_{AA}^{O1} = 0.
                                                                                                                                        (j=1, 2, 3)
    For incident P-Wave:
    G^*=G_{01},
                         G_{02} = G_{03} = G_{04} = 0
    Y_1^{01} = f_{24}k_1^2\cos^2\theta_0 + f_{23}k_1^2\sin^2\theta_0 + f_{25}m_1 + f_{26}n_1
    Y_2^{O1} = -2f_{27}k_1^2\sin\theta_0\cos\theta_0
    Y_3^{01} = im_1 k_1 \cos \theta_0
```

$$\begin{array}{l} Y_4^{01} = in_1k_1\cos\theta_0 \\ \textbf{For incident T- wave:} \\ G^* = G_{02}, \quad G_{01} = G_{03} = G_{04} = 0 \\ Y_1^{01} = f_{24}k_2^2\cos^2\theta_0 + f_{23}k_2^2\sin^2\theta_0 + f_{25}m_2 + f_{26}n_2 \\ Y_2^{01} = -2f_{27}k_2^2\sin\theta_0\cos\theta_0 \\ Y_3^{01} = im_2k_2\cos\theta_0 \\ Y_4^{01} = in_2k_2\cos\theta_0 \\ \textbf{For incident } P_o - \textbf{Wave:} \\ G^* = G_{03}, \quad G_{01} = G_{02} = G_{04} = 0 \\ Y_1^{01} = f_{24}k_3^2\cos^2\theta_0 + f_{23}k_3^2\sin^2\theta_0 + f_{25}m_3 + f_{26}n_3 \\ Y_2^{01} = -2f_{27}k_3^2\sin\theta_0\cos\theta_0 \\ Y_3^{01} = im_3k_3\cos\theta_0 \\ Y_4^{01} = in_3k_3\cos\theta_0 \\ \textbf{For incident SV-Wave:} \\ G^* = G_{04}, \quad G_{01} = G_{02} = G_{03} = 0 \\ Y_1^{01} = -(f_{24} - f_{23})k_4^2\sin\theta_0\cos\theta_0 \\ Y_2^{01} = f_{27}k_4^2\sin^2\theta_0 - f_{27}k_4^2\cos^2\theta_0 \\ Y_3^{01} = 0. \\ Y_3^{01} = 0. \end{array}$$

References

- [1] H. W. Lord, Y. Shulman, A generalized dynamical theory of thermoelasticity, *Journal of the Mechanics and Physics of Solids*, Vol. 15, No. 5, pp. 299-309, 1967.
- [2] A. E. Green, K. Lindsay, Thermoelasticity, *Journal of elasticity*, Vol. 2, No. 1, pp. 1-7, 1972.
- [3] A. E. Abouelregal, S. S. Askar, M. Marin, B. Mohamed, The theory of thermoelasticity with a memory-dependent dynamic response for a thermo-piezoelectric functionally graded rotating rod, *Scientific Reports*, Vol. 13, No. 1, pp. 9052, 2023/06/03, 2023.
- [4] S. Sharma, S. Devi, R. Kumar, M. Marin, Examining basic theorems and plane waves in the context of thermoelastic diffusion using a multi-phase-lag model with temperature dependence, *Mechanics of Advanced Materials and Structures*, Vol. 32, pp. 1-18, 07/15, 2024.
- [5] K. Sharma, M. Marin, Effect Of Distinct Conductive And Thermodynamic Temperatures On The Reflection Of Plane Waves In Micropolar Elastic Half-Space, Scientific Bulletin. Series A: Applied Mathematics and Physics. Politehnica University of Bucharest, Vol. 75, 01/01, 2013.
- [6] A. Zeeshan, M. I. Khan, R. Ellahi, M. Marin, Computational Intelligence Approach for Optimising MHD Casson Ternary Hybrid Nanofluid over the Shrinking Sheet with the Effects of Radiation, *Applied Sciences*, Vol. 13, No. 17, pp. 9510, 2023.
- [7] S. Sharma, M. Marin, H. Altenbach, Elastodynamic interactions in thermoelastic diffusion including non-local and phase lags, *ZAMM Journal of Applied Mathematics and Mechanics / Zeitschrift für Angewandte Mathematik und Mechanik*, Vol. 105, No. 1, pp. e202401059, 2025.
- [8] M. Marin, S. Sharma, R. Kumar, S. Vlase, Fundamental solution and Green's function in orthotropic photothermoelastic media with temperature-dependent properties under the Moore–Gibson–Thompson model, *ZAMM Journal of Applied Mathematics and Mechanics / Zeitschrift für Angewandte Mathematik und Mechanik*, Vol. 105, No. 6, pp. e70124, 2025.
- [9] A. Hobiny, I. Abbas, M. Marin, The Influences of the Hyperbolic Two-Temperatures Theory on Waves Propagation in a Semiconductor Material Containing Spherical Cavity, *Mathematics*, Vol. 10, No. 1, pp. 121, 2022.
- [10] R. Kumar, S. Ghangas, A. Vashishth, Wave behavior at the interface of inviscid fluid and NL biothermoelastic diffusive media, Vol. 6, pp. 11-27, 12/16, 2022.
- [11] R. Kumar, S. Ghangas, A. Vashishth, Waves at the imperfect boundary of elastic and bio-thermoelastic diffusive media, *Indian Journal of Physics*, Vol. 96, pp. 1-14, 04/01, 2021.

[12] A. K. Yadav, Effect of impedance on the reflection of plane waves in a rotating magneto-thermoelastic solid half-space with diffusion, *AIP Advances*, Vol. 10, No. 7, 2020.

- [13] M. Marin, O. Florea, On Temporal Behaviour of Solutions in Thermoelasticity of Porous Micropolar Bodies, *Analele Stiintifice ale Universitatii Ovidius Constanta, Seria Matematica*, Vol. 22, 01/10, 2014.
- [14] K. Sachin, K. Rajneesh, B. Indu, S. Gulshan, Wave propagation at free surface in thermoelastic medium under modified Green-Lindsay model with non-local and two temperature, *Structural engineering and mechanics : An international journal*, Vol. 90, No. 2, pp. 209-218, 2024. English
- [15] R. Kumar, S. Kaushal, A. Kochar, Analysis of Wave Motion in Micropolar Thermoelastic Medium Based on Moore–Gibson–Thompson Heat Equation Under Non-local and Hyperbolic Two-Temperature, *International Journal of Applied and Computational Mathematics*, Vol. 10, 03/01, 2024.
- [16] R. Kumar, D. Batra, S. Sharma, Thermoelastic medium with swelling porous structure and impedance boundary under dual-phase lag, *Engineering Solid Mechanics*, Vol. 13, pp. 81-92, 01/01, 2025.
- [17] X. Li, C. Li, Z. Xue, X. Tian, Analytical study of transient thermo-mechanical responses of dual-layer skin tissue with variable thermal material properties, *International Journal of Thermal Sciences*, Vol. 124, pp. 459-466, 2018/02/01/, 2018.